Localization due to topological stochastic disorder in active networks

Dekel Shapira, Dganit Meidan, Doron Cohen

Department of Physics, Ben-Gurion University of the Negev, Beer-Sheva 84105, Israel

An active network is a prototype modeling of a system where the 'particles' have a self-propulsion mechanism. We highlight the emergent aspect of *topological stochastic disorder* (TSD), and discuss its consequences. We illuminate 3 different routes to under-damped relaxation: (a) delocalization of a relaxation mode due to drift; (b) topological symmetry breaking of a relaxation mode; (c) TSD-induced mixing of different relaxation modes. The localization of the relaxation modes due to TSD plays a major role in the analysis. This type of novel non-Hermitian localization is very different from the conservative Anderson-type localization.

I. INTRODUCTION

Gas that consists of particles that perform self-propelled stochastic motion is a novel paradigm in statistical mechanics [1–4]. We are interested in the implications of disorder, and the possible manifestation of localization effect in the relaxation modes of such systems. Consider for example a system that consists of Janus particles [5–7]. Those are spherical-like nanoparticles ($\sim$100nm size), coated at each of their two hemispheres with different materials. Immersed in solution, and radiated with light, they produce self-propelled motion. Fig.1(a) shows a caricature of a Janus particle in one-dimensional system. Such system can be 'disordered' due non-homogeneity of the background environment, or because of the non-homogeneity of the illumination. It is the latter type of disorder which we find intriguing, since it has to do with the self-propulsion mechanism. As explained below such type of disorder is *topological* rather than *conservative*.

We consider a minimal configuration for such self-propelled particle in a random environment. Namely, we assume that the dynamics takes place on a quasi one-dimensional grid, see Fig.1(b). If the particle is facing the right, we say it has positive helicity. If its black-white orientation is opposite, we say that it has negative helicity. Accordingly, its states $|n, y\rangle$ are defined in terms of position ($n =$ integer) and spin coordinate ($y = \uparrow, \downarrow$). Below we refer to the system as 'lattice' that consists of 'sites'. Each two sites with the same index n form a 'cell', and two adjacent cells, along with their connecting bonds, form a 'tile'. The dynamics is described by a stochastic rate equation

$$\frac{d}{dt}\boldsymbol{p} = \boldsymbol{W}\boldsymbol{p} \tag{1}$$

where $\boldsymbol{p}$ is vector of probabilities, and the off-diagonal elements of the $\boldsymbol{W}$ matrix are the transition rates w (with an appropriate bond index). The diagonal elements $-\gamma$ (with an appropriate state index) are implied by conservation of probability (the sum of each columns has to be zero). The matrix $\boldsymbol{W}$ is given explicitly in Appendix A. The rate of transition between two sites, connected by a
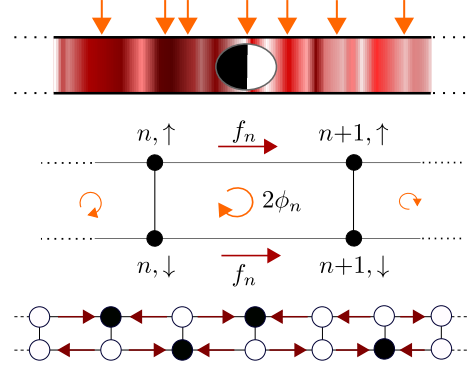

FIG. 1. **Model geometry. (a)** A Janus particle in 1D random environment. The non-uniform illumination(arrows) induce self-propulsion in the direction of the head (white semi circle). **(b)** One tile of the lattice is plotted. The ring consists of N tiles with periodic boundary conditions. The transition rates along the vertical bonds are $w=1$ in both directions, representing random flips of the self-propelled motion ('helicity'). The horizontal bonds are biased: the stochastic field there ($\mathcal{E}$) is written as the sum of a drift (f_n) and a self-propulsion term (ϕ_n). The four parameters of the model are: the average drift ($\bar{f}$); its non-uniformity (σ_f); the average propulsion ($\bar{\phi}$); and the topological disorder (σ_ϕ). The latter reflect that we are dealing with an active network. **(c)** An illustration for a representative segment of the lattice. The black sites are those that serve as sinks for the stochastic flow in the presence of strong disorder. They support the floor-level relaxation modes.

bond (b), is characterized by a stochastic field

$$\mathcal{E}_b = \ln\left(\frac{w_{\vec{b}}}{w_{\overleftarrow{b}}}\right) \tag{2}$$

whose sign indicates the preferred sense of transition. Thus the rates on a given bond can be written as $w_b \exp(\pm\mathcal{E}_b/2)$. In the geometry of Fig.1(b), the vertical bonds represent random flip of helicity, and therefore are characterized by a zero stochastic field. In contrast the horizontal bonds are biased. The stochastic field on the bond $b = (n, y)$ that connects node $|n, y\rangle$ to $|n+1, y\rangle$ is conveniently written as a sum of drift and self-propulsion terms, namely,

$$\mathcal{E}_{n,\uparrow} = f_n + \phi_n \tag{3}$$
$$\mathcal{E}_{n,\downarrow} = f_n - \phi_n \tag{4}$$

Type	aka	Relevant models	Comments
Type-I	Diagonal disorder	Anderson model (random potential)	Might have a mobility edge
Type-II	Bond disorder	Debye model; Random-resistor-network	Might lead to a percolation transition
MFD	Phase Disorder	Anderson with random vector potential	The topological aspect is not pronounced
CSD	-	Sinai model of random stochastic transitions	Reduces to type-I via a gauge transformation
RSD	Sign Disorder	Random excitatory and inhibitory connections	non-hermiticity cannot be gauged away
TSD	-	Generic active networks	non-hermiticity is of topological origin

TABLE I. Different types of disorder.

The activity of the network is reflected in having non-zero circulations, aka affinities (analogous to magnetic field). The circulation of the n-th tile is $\mathcal{B}_n = 2\phi_n$. If all the circulations are zero, a gauge transformation can be used in order to show that $\boldsymbol{W}$ is similar to a symmetric matrix $\boldsymbol{H}$, hence all the eigenvalues are real, as for hermitian Hamiltonians. Otherwise we are dealing with the physics of non-hermitian matrices, where the spectrum might become complex [8–19]

Model parameters.– The motion of the Janus particles of Fig.1 can be biased either due to a non-zero average drift field $\bar{f}$, or due to a non-zero average self-propulsion $\bar{\phi}$. Disorder may arise due to the non-homogeneity of the background environment, or due to the non-homogeneity of the illumination source. Respectively, we distinguish between *conservative stochastic disorder* (CSD) for which the f_n acquire a random term $\in [-\sigma_f, \sigma_f]$, and *topological stochastic disorder* (TSD) for which the ϕ_n acquire a random term $\in [-\sigma_\phi, \sigma_\phi]$.

A. Related studies

The topological nature of the NESS for the model that we are considering, without disorder, has been discussed in [20, 21], and a connection has been established with the Su-Schrieffer-Heeger model following the work of [22] on topological boundary modes in isostatic lattices. In the present work we are not considering the NESS, but rather the relaxation modes, and their bulk localization properties due to disorder. We note also that the NESS of similar non-disordered quasi-one-dimensional models has been investigated in the context of traffic with exclusion rules, see for example [23, 24]. The main focus in the latter case was the formation of a polarization wall due to the entering and the exiting rates at the boundaries.

It is customary to distinguish between two types of disorder, so called Type-I and Type II [25, 26]. We explain these terms in the present context, and highlight new type of disorder that has not been illuminated so far. The different types of disorder are summarized in Table I.

Random f_n, as in the Sinai model (aka random walk in random environment) [27–30], translates, under gauge-like transformation, into Type-I disorder [12], which is a diagonal on-site disorder as in the Anderson model (electron in a random potential). We shall call it below *conservative stochastic disorder* (CSD).

Random w_b, as in random resistor network models [31], or as in the Debye model (balls connected by non-identical springs), translates into Type-II disorder, which is an off-diagonal bond disorder. The latter type of disorder can lead to a percolation-like transition that affects the relaxation modes [17], and we shall not consider it further.

In the present work we consider a new type of disorder that we call *topological stochastic disorder* (TSD). This type of disorder originates from having random ϕ_n, and unlike CSD, cannot be gauged-away. We note that physically, TSD arises naturally also in situations other than active particles. For example the affinities $\mathcal{B}_n$ may reflect non-conservative drift-fields that are induced by electro-motive-forces.

With the substitution $\phi_n \mapsto i\phi_n$ our TSD becomes magnetic-field-disorder (MFD) that has been discussed in the past, e.g. [32] and references therein. One should be aware that there is an essential difference between TSD and MFD: the latter has qualitatively the same effect as the usual Type-I Anderson disorder, while TSD makes the spectrum complex.

Another meaningful comparison is between the TSD and the random sign disorder (RSD) of [16]. The latter concerns non-Hermitian localization in biological networks, where the w_b have random sign, corresponding to random excitatory and inhibitory connections. It should be realized that RSD has nothing to do with topology: the model of [16] is a single channel tight binding model with near-neighbor transitions. In contrast, TSD requires at least two channels, as in the case of a random magnetic field. Also it should be realized that it is not possible to control the strength of RSD: once it is introduced the spectrum becomes complex, while for TSD we shall see that the percentage of the complex eigenvalues, and their dispersion, is tunable.

B. Outline

The relaxation modes are the right eigen-vectors of $\boldsymbol{W}$. They are associated with eigenvalues $\{-\lambda_r\}$ that can be either real or come in complex-conjugate pairs, corresponding to over-damped or under-damped relaxation,

respectively. In Section II we demonstrate that an active network can exhibit 3 routes to complexity (underdamped relaxation): (a) delocalization of a relaxation mode due to drift; (b) topological symmetry breaking of a relaxation mode; (c) TSD-induced band-mixing of real relaxation modes.

In Section III we provide the detailed account for the symmetry-breaking mechanism in the absence of disorder. We emphasize that self-propulsion makes the spectrum partly-complex, exhibiting 'exceptional points'. See [8, 9] for an introduction for the physics of non-hermitian degeneracies. In Section IV we explain how the spectrum is affected by the introduction of TSD, and why the threshold for complexity diminishes due to the disorder.

In Section V we introduce several measures for the characterization of a relaxation mode: the number of lattice sites that support the mode (M); the number of floor-level sites that are involved (Q); their polarization (D); their localization lengths (L); and the effective circulation that they experience (B). These measures help to gain a deeper insight into the spectrum.

As will be shown later, CSD is responsible to the robustness of reality, meaning that eigenvalues remain real even if not-too-strong circulations are introduced. In contrast TSD leads to complexity via topological mixing. But there is a twist: we observe in Section VI that strong stochastic disorder, irrespective of its nature, induces "lattice dilution", leading to the formation of a *floor-level*. Consequently the effective dimensionality of the lattice reduces, and a robust reality is gained within this floor-level. The topological-index perspective of the disorder, and its connection to the floor level phenomenology is further discussed in Section VII.

Two routes to complexity, the symmetry-breaking route and the TSD band-mixing route, reflect that we are dealing with an active network. These mechanisms are local is some sense, and are not associated with global delocalization of the eigen-modes. In the concluding Section VIII we re-phrase some of our insights using a physically illuminating language.

II. DIFFERENT ROUTES TO COMPLEXITY

We first remind the reader the simplest result for the relaxation spectrum of particles that diffuse in a single-channel biased ring. This result illustrates the *delocalization route to complexity*. For any non-zero bias the spectrum becomes fully complex $\lambda = Dk^2 + ivk$, where k is the wave-number, D is the diffusion coefficient, and v is the drift velocity. Similar expression applies for a tight binding model, see e.g. [18]. If stochastic disorder is added, the complexity appears only if the bias exceeds a finite threshold, aka delocalization threshold [10, 11]. As discussed in [18] the low relaxation modes (small Re[λ]) get delocalized first, while the high lying relaxation modes remain real.

We consider a two-channel ring of N unit cells with periodic boundary conditions (Fig.1(b)). This is the simplest example for an active network, and we are going to find two additional routes to complexity that have to do with the non-trivial topology of the model. We distinguish between the circulation that is induced by the drift, and the circulation that reflects the self-propulsion, namely,

$$S_f = \sum f_n \equiv N\bar{f} \tag{5}$$

$$S_\phi = \sum \mathcal{B}_n \equiv 2N\bar{\phi} \tag{6}$$

where $\mathcal{B}_n = 2\phi_n$ is the affinity of the n-th tile. For simplicity we assume that all the couplings are identical ($w_b = 1$ for any b). In the absence of disorder, $\boldsymbol{W}$ is translationally symmetric and can be written very simply using momentum and spin operators:

$$\boldsymbol{W} = (\boldsymbol{\sigma}_x - 1) + \sum_\pm e^{\pm\frac{1}{2}\left(\bar{f}+\bar{\phi}\boldsymbol{\sigma}_z\right)}\left(e^{\mp i\boldsymbol{p}} - 1\right) \tag{7}$$

The Pauli operator $\boldsymbol{\sigma}_x$ term induces the random change in the propulsion direction (vertical transitions in Fig.1), the $\pm$ terms generate the forward and backward transitions, while the "-1" terms provide the diagonal elements ("decay rates") that are required for conservation of probability. The operators $e^{\pm i\boldsymbol{p}}$ and $\boldsymbol{\sigma}_i$ are written using explicit Dirac notations in Appendix A.

We are now in position to explain how each of the parameters in the model affects the complexity of the spectrum.

CSD.– Conservative stochastic disorder arises if all the ϕ_n are zero while the $f_n \in [-\sigma_f, \sigma_f]$ have finite dispersion and zero average. Such type disorder can be derived from a stochastic potential that features activation barriers, as discussed by Sinai and followers [27]. The asymmetry of the $\boldsymbol{W}$ matrix can be gauged away, hence it is similar to an hermitian matrix, and the relaxation spectrum comes out real. The corresponding eigenstates are Anderson-localized.

Propulsion.– Without disorder the relaxation spectrum can be found analytically (see Section III). Adding self propulsion $\bar{\phi}$, unlike drift, leads to a very different route to complexity, that is not related to delocalization of the eigenstates. For low self-propulsion the spectrum remains real, while above some critical value the relaxation modes undergo a symmetry-breaking transition. Consequently a circle of complex eigenvalues appears. In Fig.2 this circle is indicated by a solid line. If we add weak stochastic disorder the spectrum is blurred, as illustrated in Fig.2 for TSD, and in Fig.3(a) for CSD.

TSD.– Another route to complexity has to do with mode mixing due to TSD. Even if the propulsion is zero on the average, we still can have finite dispersion $\phi_n \in [-\sigma_\phi, \sigma_\phi]$. Then the problem becomes non-Hermitian in a very essential way, and part of the spectrum becomes complex. This is illustrated in Fig.3(b), where we turn off the propulsion for the system of Fig.2, but keep the TSD. It should be clear that if we turn off

the propulsion for the system of Fig.3(a) the complexity vanishes and we get a real spectrum.

Drift.– Without disorder, finite non-zero drift $\bar{f}$ has the same effect as for a single-mode ring, leading to delocalization of the spectrum. We demonstrate in Fig.3(c,d) the drift-induced delocalization route to complexity. The
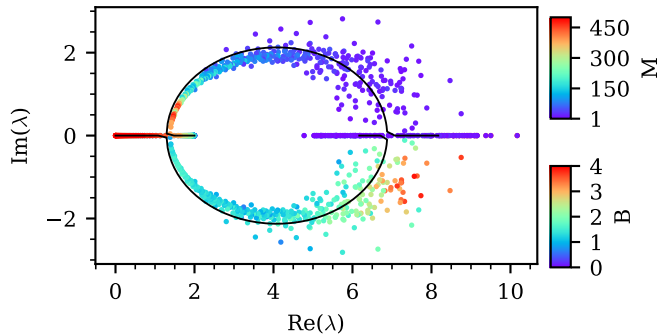

FIG. 2. **Representative relaxation spectrum.** The spectrum for finite propulsion ($\bar{\phi} = 2$) and TSD ($\sigma_\phi = 1$) with $n = 500$. The eigenvalues are presented in the complex plane. Each associated eigen-mode is characterized by various measures: The real and Im[λ] > 0 points are color-coded by the participation number M, while the conjugate Im[λ] < 0 points are color-coded by the effective propulsion B. See text for definitions. The solid line illustrates the spectrum of the non-disordered system Eq.(13).
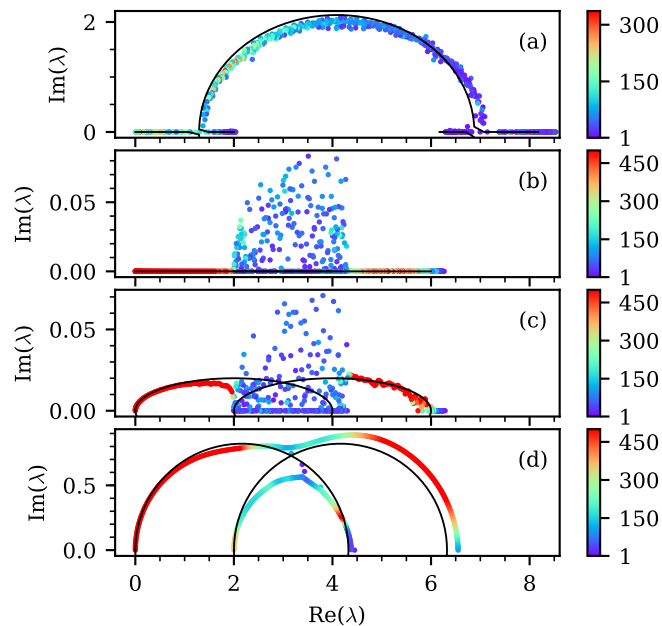

FIG. 3. **Representative relaxation spectra.** Same presentation as in Fig. 2; conjugate eigenvalues excluded. **(a)** Same propulsion as in Fig.2, but with CSD ($\sigma_f = 1$) instead of TSD. **(b)** Same TSD as Fig.2, but the average propulsion is zero. **(c)** Same as (b), but with weak drift ($\bar{f} = 0.02$). **(d)** Same as (b), but with stronger drift ($\bar{f} = 0.8$).

drift can delocalize the lower (small Re[λ]), and possibly also the upper (large Re[λ]) part of the spectrum, where we have single mode physics. We also see the interplay of the drift and the TSD in the middle part of the spectrum where the two channels overlap. For strong drift the TSD induces an avoided crossing, while for weak drift the TSD-induced complexity predominates.

III. TOPOLOGICAL SYMMETRY BREAKING

The $\boldsymbol{W}$ matrix formally operates above an Hilbert space of states whose standard representation is

$$|\psi\rangle = \sum_{n,y} \psi_{n,y} |n, y\rangle \tag{8}$$

The right eigenvectors of $\boldsymbol{W}$ are the relaxation modes of the network. The eigenvector that corresponds to the zeroth eigenvalue $\lambda_0 = 0$ is the non-equilibrium steady state (NESS), while all the the other eigenvalues are written as $\{-\lambda_r\}$, with Re[λ_r] > 0.

For our geometry, beside the NESS, there is another special mode with the eigenvalue $\lambda=2$. This can be seen by considering the left eigenvector $|\tilde{2}\rangle = \sum_n (|n,\uparrow\rangle - |n,\downarrow\rangle)$. All the $\lambda \neq 2$ eigen-modes are orthogonal to this special left eigenvector, hence the sum $\sum_n \psi_{n,y}$ has to be equal for positive and negative helicities. Consequently it is implied that the NESS has equal weight for clockwise and anticlockwise motion, while for all the relaxation modes the sum of amplitudes vanishes for each direction. The same considerations also give the time-dependence of the total polarization

$$D = \sum_n D_n = \sum_n (p_{n,\uparrow} - p_{n,\downarrow}) \tag{9}$$

Multiplying Eq.(1) from the left with $|\tilde{2}\rangle$, one obtains a universal decay law $\dot{D} = -2D$.

In the absence of disorder the $\boldsymbol{W}$ matrix is block-diagonal in the basis $|k, y\rangle$, where k is the wave-number. For $\bar{\phi} = \bar{f} = 0$ the spectrum consists of two bands along the real axis, namely, $\lambda_{k,+} = 2 + 2\cos(k)$ and $\lambda_{k,-} = 4 + 2\cos(k)$. The existence of the 2-channel topology is reflected by having an overlap $2 < \lambda < 4$. Note also that all the eigenvalues are doubly degenerate due to $k \mapsto -k$ symmetry. This holds true also for $\bar{\phi} \neq 0$ (we still keep $\bar{f} = 0$). But now the spectrum becomes complex. The k-th block of the $\boldsymbol{W}$ matrix is

$$\boldsymbol{W}^{(k)} = b\boldsymbol{\sigma}_x - ia\boldsymbol{\sigma}_z + c\mathbf{1} \tag{10}$$

where $b = 1$, and

$$a = \left[2\sinh\left(\frac{\bar{\phi}}{2}\right)\right]\sin(k) \tag{11}$$

$$c = \left[2\cosh\left(\frac{\bar{\phi}}{2}\right)\right]\cos(k) - \left[1 + 2\cosh\left(\frac{\bar{\phi}}{2}\right)\right] \tag{12}$$

The matrix above is similar to a real matrix $b\boldsymbol{\sigma}_z - ia\boldsymbol{\sigma}_y$. Such matrices are usually encountered if there is an anti-unitary symmetry such as "T" or "PT" [8, 9]. However we shall stick with the physical representation of Eq. (10). The eigenvalues are either real or come in complex-conjugated pairs, namely,

$$\lambda_{k,s} = -\left[c \pm \sqrt{b^2 - a^2}\right] \tag{13}$$

where $s = 1, 2$ labels the lower and upper band respectively. The spectrum is real for $|a| < |b|$ and complex for $|a| > |b|$. The latter possibility is realized if $2\sinh(\bar{\phi}/2) > 1$, leading to a critical value for self-propulsion:

$$\phi_c \approx 0.96. \tag{14}$$

Fig.2 shows a representative spectrum for $\bar{\phi} > \phi_c$, where the solid line is based on Eq.(13).

The eigen-modes are labeled as $|k, s\rangle$. In the Bloch sphere representation they reside in the XY or in the YZ plane, depending on whether they are associated with real or complex eigenvalues, respectively. Close to the so-called exceptional point ($a = b$) they coalesce into the same Y direction. Disregarding normalization, the eigen-modes are

$$|k, s\rangle = \sum_n e^{ikn}\left(|n, \uparrow\rangle \pm e^{\pm i\varphi}|n, \downarrow\rangle\right) \tag{15}$$

where $\tan(\varphi) = q/\sqrt{1 - q^2}$, with $q = a/b$. We see that self-propulsion with large q makes φ imaginary, and consequently the symmetry with respect to the helicity is broken, and the modes become helical, meaning that clockwise modes are separated from anti-clockwise modes. On top we note that the $|k, s\rangle$ have a systematic degeneracy for $k \mapsto -k$.

The spectrum of the non-disordered model is further analyzed in Appendix B, and is illustrated in a few representative cases in Fig.4. It is composed of two bands. As discussed above, in the absence of f the bands are deformed into the complex plane provided $\phi > \phi_c$. Panels (a-c) illustrate this deformation for increasing values of ϕ. It is important to notice that the $\pm k$ symmetry is not broken, hence each of the two $-\lambda_{k,s}$ trajectories is degenerated and encloses a zero area. This is no longer true of if we add a non-zero f. In the latter case the $\pm k$ degeneracy is removed, and the $\lambda_{k,s}$ trajectories encloses a finite area.

IV. THE INTRODUCTION OF TSD

We now consider what happens if the illumination is non-uniform. Thus we have TSD with some variation σ_ϕ on top of the average value $\bar{\phi}$. At this point one may wonder whether it is feasible to introduce TSD with *zero* average propulsion (the illuminated particles in Fig.1 are always self-propelled in the direction that they are facing). After little reflection one realizes that it is possible
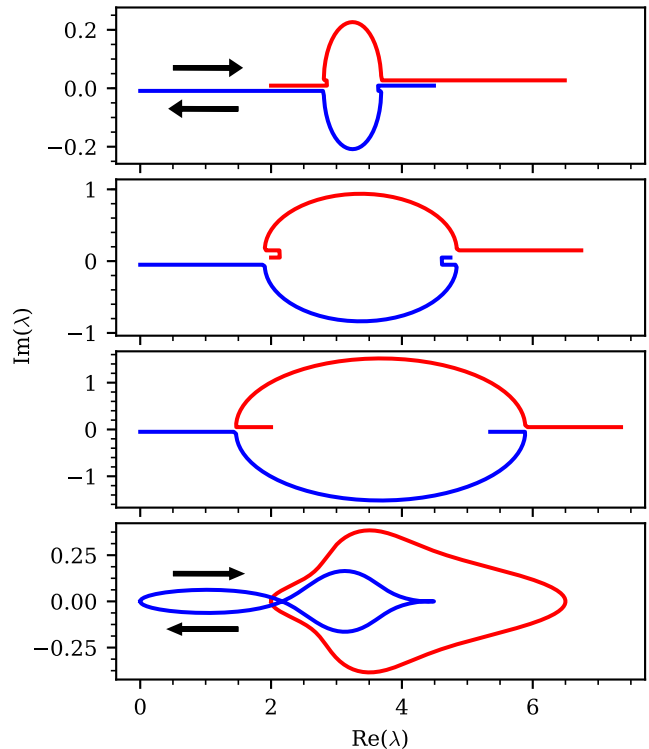

FIG. 4. The Bloch spectrum $\lambda_{k,s}$. The two bands are $s = 1$ (blue) and $s = 2$ (red). In panels (a) to (c) we have $\phi = 0.98, 1.2, 1.6$, while $f = 0$. Note that $\phi_c \approx 0.96$. Eq.(13) has been used. For presentation purpose the horizontal pieces of the band have been shifted off the real axis. Panel (d) is for the same ϕ as in (a), but with an added $f = 0.01$ that lifts the $\pm k$ degeneracy. The black arrows show the direction in which λ_k is changing as $k \in [0, 2\pi]$ is increased from zero, and eventually comes back.

to introduce such TSD if the black-white coating of the particle is reversed in its lower half. Then one can use two sources of illumination: upper illumination source that induces self-propulsion to the right, and a lower illumination source that induces self-propulsion to the left. If the two sources are of equal average intensity, the combined effect is to have *zero* average propulsion, and hence unbiased TSD.

Let us see how the diagonalization procedure for $\boldsymbol{W}$ is affected in the presence of non-uniform illumination, without assuming any restrictions on the values of $\bar{\phi}$ and σ_ϕ. The standard site-basis is $|n, y\rangle$. In order to get rid of the vertical coupling we can switch to the basis $|n, \pm\rangle$, where $\pm$ are the modes that are defined by $\boldsymbol{\sigma}_x$. In the absence of propulsion (or TSD) we get two non-interacting chains, see illustration in Fig.5. Each chain can be diagonalized hence we go to the basis $|k, \pm\rangle$. If we introduce disorder and neglect the inter-band couplings, the spectrum is still real, and can be labeled $|\alpha, \pm\rangle$. The α-states unlike the k-states are not 'free waves' and become localized as disorder is increased. In the $|\alpha, \pm\rangle$ basis we can
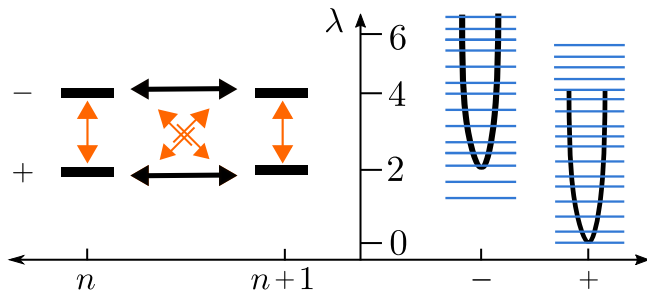
FIG. 5. **Diagonalization procedure.** We go from the site-representation $|n, y\rangle$ of Fig.1(b) to the mode representation $|\alpha, \pm\rangle$, which is illustrated on the left. The diagonal arrows represent anti-hermitian couplings due to self-propulsion. The thick double-sided arrows represent the hermitian hopping elements between cells. The disorder affects all those couplings, and also adds vertical hopping elements. The unperturbed diagonal 'energies' are $\lambda = 2$ and $\lambda = 4$. With hopping we get two bands $[0, 4]$ and $[2, 6]$ that are illustrated by solid line on the right. Neglecting the inter-band couplings the spectrum is still real, represented by the blue vertical segments. The complex spectrum appears due to band mixing, as explained in the main text.

write

$$\boldsymbol{W} = \boldsymbol{H} + \boldsymbol{A}, \tag{16}$$

where $\boldsymbol{H}$ is hermitian, and $\boldsymbol{A}$ is an anti-hermitian matrix due to the self-propulsion. The disorder-induced hermitian and anti-hermitian couplings are represented, respectively, by the vertical and diagonal arrows in Fig.5.

In the absence of disorder $\boldsymbol{A}$ couples only states with the same k, hence $\boldsymbol{W}$ takes the block-diagonal form Eq. (10) where $\boldsymbol{A} = ia\boldsymbol{\sigma}_z$ are the anti-hermitian inter-band couplings. Then we get the Bloch eigenstates $|k, s\rangle$ where $s = 1, 2$. With weak TSD the matrix $\boldsymbol{W}$ is no longer block-diagonal. Rather $\boldsymbol{A}$ becomes banded. It does not require strong disorder in order to induce band mixing. The condition for band mixing is to have $\boldsymbol{A}$-couplings that are larger compared with the level-spacing. This is a very easy condition which is implied by perturbation theory, see Appendix C. Consequently very weak disorder is enough to induce complexity within the range $2 < \mathrm{Re}[\lambda] < 4$. We note that the appearance of disorder-induced hermitian couplings in $\boldsymbol{H}$ of Eq.(16) does not change this picture: it scramble the levels of the two bands, but does not alter much their density in the overlap region.

The explanation above illuminates why uniform ϕ_n, unlike random ϕ_n that has the same average intensity, requires a finite threshold Eq. (14) in order to induce complexity in the spectrum. Fig.6 displays how the overall fraction of complex eigenstates depends on σ_ϕ, while Fig.7 shows their percentage within the range $2 < \lambda < 4$. Section VI will provide a detailed discussion of both figures.
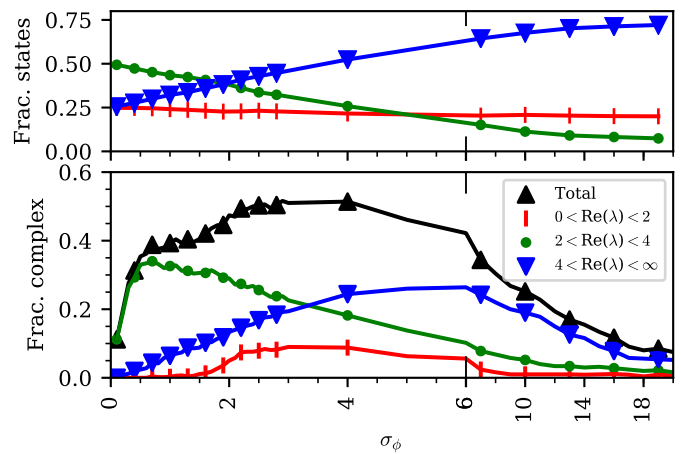

FIG. 6. **The spectral distribution of the eigenvalues. (a)** The fractions of eigenvalues per spectral window versus σ_ϕ, while the average propulsion is zero. **(b)** The fraction of complex eigenvalues (out of all eigenvalues), divided into the different spectral windows. In some realizations of the system there are residual complex eigenvalues in the first window ($\mathrm{Re}[\lambda] < 2$), with small imaginary part. It is not clear whether these are numerical issues or not. The threshold for complexity here is $\mathrm{Im}[\lambda] > 10^{-4}$. The plots are for rings of $N = 500$ cells. Each point is one realization, and all the realizations have the same random seed.
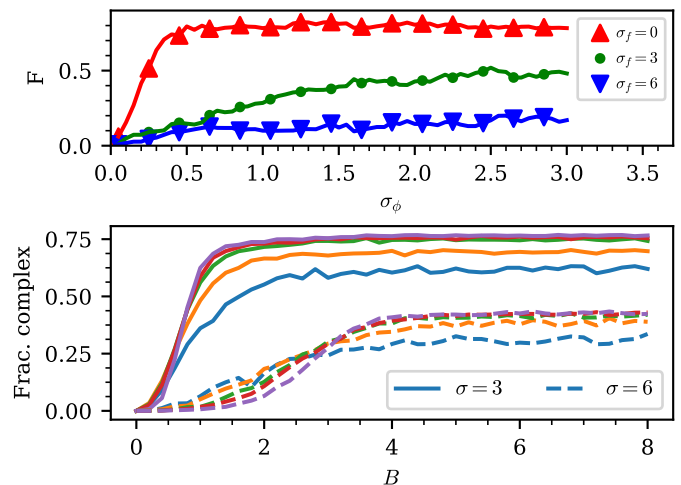

FIG. 7. **The fraction of complex eigenvalues. (a)** The fraction of complex eigenvalues relative to the number of eigenvalues in the second window ($\mathrm{Re}[\lambda] \in [2, 4]$), for different σ_f. For larger CSD, the fraction becomes smaller. **(b)** The total fraction of complex eigenvalues for a simple ring. Each point in the plots is averaged over 100 realizations. The solid and dashed lines are respectively for $\sigma=3$ and $\sigma=6$. The different lines (from bottom to top at $B > 4$) are for rings of length $L = 5, 10, 20, 30, 60$.

V. TOPOLOGICAL CHARACTERIZATION OF THE EIGEN-MODES

Assuming square-integrable normalized eigenstates we formally define $P_{n,y} = |\psi_{n,y}|^2$ and $P_n = \sum_y P_{n,y}$, such that $\sum P_n = \sum P_{n,y} = 1$. Additionally we define, using an harmonic average, a topological weight for each tile:

$$P_n^* = 8 \left[\sum_{\text{site} \in n} P_{n,y}^{-1} \right]^{-1} \qquad (17)$$

where site $\in n$ refers to the 4 sites from which the n-th tile is formed. The prefactor is chosen such that $P_n^* = 1/N$ for a uniform occupation. A vanishingly small P_n^* means that the n-th cell does not form a closed ring.

It is now possible to introduce several measures that characterize a given eigen-modes:

$$M = \left[\sum_{n,y} P_{n,y}^2 \right]^{-1} \qquad (18)$$

$$L = \left[\sum_n P_n^2 \right]^{-1} \qquad (19)$$

$$L^* = L \sum_n P_n \qquad (20)$$

$$Q = \sum_{(n,y)\in\text{floor}} P_{n,y} \qquad (21)$$

The first two measures characterize the volume that is occupied by the eigen-modes: M is the number of sites that participate in the formation of the eigen-mode, while L is the respective localization length. The topological localization length L^* is further discussed below. The definition and the significance of Q will be discussed in the next section.

It is important to realize that the eigenstates might be helical, meaning that $P_{n,\uparrow} - P_{n,\downarrow}$ is not zero. Helicity can arise either due to symmetry breaking, as discussed in Section III, or due to the formation of a floor-level, which is discussed in the next section. For a strictly helical eigenstate $L = M$ as opposed to $L = M/2$. Numerical results for M and L and L^* are presented in Fig.8(d).

The topological localization length L^* reflects the effective circulation which is experienced by a given eigen-mode. It is determined by the total topological weight $\sum P_n^*$, which is the occupation probability of the region that experiences propulsion. If the total topological weight is much smaller than unity, it means that the non-hermiticity can be gauged away from the volume that supports the eigenmode, hence the eigenvalue is real (or with very small imaginary part). If the total topological weight is non negligible, it makes sense to define the effective circulation that is experienced by the eigen-mode as follows:
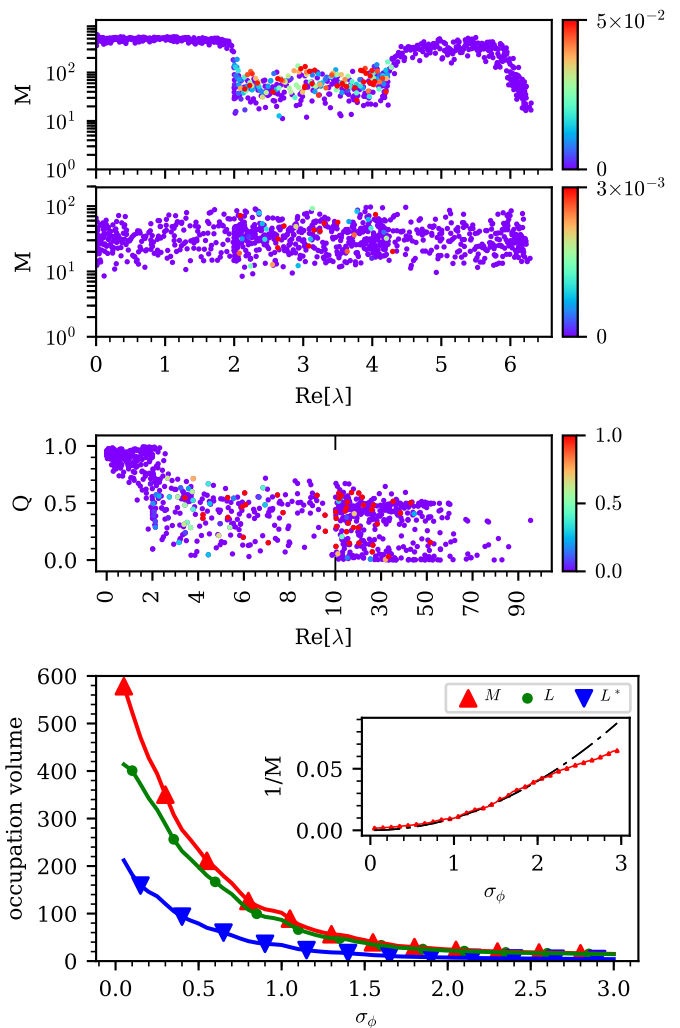
$$B = \sum_n P_n \mathcal{B}_n \qquad (22)$$

FIG. 8. **The participating sites for each eigenmode.** **(a)** The participation number M versus $\text{Re}[\lambda]$ for $\sigma_\phi = 1$ and $\sigma_f = 0.1$. **(b)** Same as (a) but with the disorder parameters reversed: $\sigma_f = 1$ and $\sigma_\phi = 0.1$ **(c)** The floor-level occupation Q versus $\text{Re}[\lambda]$ for $\sigma_\phi = 8$. **(d)** The various occupations volumes versus σ_ϕ. In (a) and (b) the points are color coded by $\text{Im}[\lambda]$. In (c) each point is an average over all the eigenstates within $2 < \text{Re}[\lambda] < 4$. The inset shows that the inverse localization length has roughly quadratic dependence on the disorder strength, as in the Anderson model.

In the absence of disorder, the eigen-modes are uniform, and and we get $B = 2\bar{\phi}$. In the presence of disorder, the eigen-modes get localized, but if they are uniform within the localization volume (with zero helicity) we still get $B \approx 2\bar{\phi}$. On the other extreme, if the eigen-modes are completely helical we get a vanishing B. For intermediate situation, where the eigen-mode is supported partially by topologically connected cells, and partially by dangling sites, the bare $2\bar{\phi}$ is multiplied by the total topological weight of the eigen-mode.

The effective circulation for each state in Eq.(22) can be estimated using the measures L and L^* as follows:
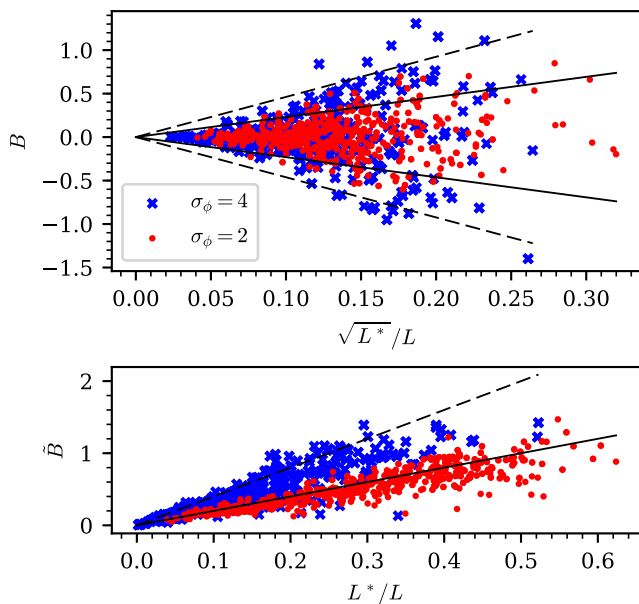
FIG. 9. **(a)** The effective circulation B of the eigenstates versus their $\sqrt{L^*}/L$, calculated for TSD with $\sigma_\phi = 2$ (red) and $\sigma_\phi = 4$ (blue). The solid and dashed lines are given by Eq.(23). **(b)** We define $\tilde{B} = \sum_n P_n|\mathcal{B}_n|$ and verify that it agrees with the estimate $\sim (L^*/L)\sigma_\phi$. Both panels refer to the same set of eigenstates, namely, those that reside in the spectral window $2 < \text{Re}[\lambda] < 4$.

By definition, $\sum P_n = L^*/L$. There are L^* terms in the sum, accordingly each term can be estimated as $\sim 1/L$. It follows that B is normally distributed with zero mean and standard deviation

$$\text{Std}(B) = \frac{\sqrt{L^*}}{L}\text{Std}(\mathcal{B}_n) = 2\frac{(2\sigma_\phi)}{\sqrt{12}}\frac{\sqrt{L^*}}{L} \quad (23)$$

This estimate is tested in Fig.9. We conjecture that B affects the complexity of the eigen-mode. A hand-waving argument that supports this conjecture goes as follows: All the asymmetric transition of dangling bonds can be gauged away using a similarity transformation; hence $\boldsymbol{W}$ is similar to a matrix $H + A$ where H is real and symmetric, while the anti-symmetric matrix A is supported only by the topologically connected cells. Multiplying $\boldsymbol{W}\psi = \lambda\psi$ from the left by $\psi^\dagger$ we deduce that $\text{Im}[\lambda] = \sum A_{ij}\text{Im}[\psi_i^*\psi_j]$. Consequently we conclude that from statistical perspective $\text{Im}[\lambda]$ is proportional to the topological weight of the eigen-mode.

The above conjecture provides a qualitative explanation for the remarkable difference between TSD and CSD in Fig.2 and Fig.3(b) respectively. The transverse scattering of the complex eigenvalues in the former case becomes larger as the localization volume M becomes smaller. Modes with larger B experience (by definition) a larger effective propulsion, and therefore they are pushed to a larger radius. CSD, unlike TSD, does not have a systematic (M dependent) effect on B, because the $\mathcal{B}_n$ are the same for all cells.

The dependence of L on the strength of the disorder is important for the understanding of Fig.7(a) where we plot the fraction F of complex eigenvalues due to topological band-mixing. As already clarified in the previous section, very weak disorder is enough to make $\boldsymbol{A}$ in Eq.(16) banded, and hence to induce complexity in the spectrum. On the basis of standard Fourier-analysis argumentation the bandwidth of $\boldsymbol{A}$ is determined by the inverse localization length $1/L$, which is like uncertainty in k. Thus Fig.7(a) can be regarded as a reflection of the L dependence in Fig.8(a). One can also wonder what determines the complexity saturation value of F. For one dimensional rings that were studied in [17] an analytical treatment has been introduced: for stronger disorder the saturation value becomes smaller, and the approach to this value is smeared, as illustrated in Fig.7(b). To test that our qualitative understanding of F is indeed correct, we show in Fig.7(a) how F is affected by adding CSD. Increasing σ_f unlike increasing σ_ϕ affects the saturation value. The analogy here is as follows: the σ_f of CSD is by definition the σ disorder in a one dimensional ring, while the σ_ϕ of TSD controls the effective B and hence analogous to the affinity of the one dimensional ring. It is true that further increase of σ_ϕ affects the L of the eigenstates too, but this has almost no implication. To see why, we illustrate in Fig.7(b) how the F of a simple ring is affected by its length L, which plays the role of localization length in the model under study.

VI. THE FORMATION OF THE FLOOR LEVEL

In the presence of strong disorder the NESS is mainly supported by the floor-level sites that serve as "sinks" for the probability flow. See Fig.1(c) for illustration. The low lying relaxation modes mainly occupy the same sites. This hypothesis is established by Fig.8(b), where we plot the floor occupation Q that has been defined in Eq.(21).

In Fig.6(a) we show how the eigenvalues are distributed with respect to $\text{Re}[\lambda]$. Generally speaking we see that the spectrum is stretched upward along $\text{Re}[\lambda]$. This can be easily explained noting that the diagonal elements of the $\boldsymbol{W}$ matrix become very large for strong disorder. Namely,

$$\gamma_{n,y} = 1 + e^{\phi_n/2} + e^{-\phi_{n-1}/2} \quad (24)$$

But a careful look reveals that within $\text{Re}[\lambda] \in [0, 2]$ we have an approximate 25% fraction of real eigenvalues, irrespective of the TSD strength. The 25% is not surprising in the limit of weak disorder: their reality is implied by the band structure. But their presence and reality persist also for very strong disorder due to the formation of the floor level. From Eq.(24) it follows that for sink site $1 < \gamma < 3$. Furthermore, as the disorder is increased $\gamma \to 1$. The hopping between the floor-level states (via high lying states) leads to the formation of the floor-level band, as established by Fig.8(c). If we have TSD only, the fraction of floor-level sites is 25%. Adding propulsion
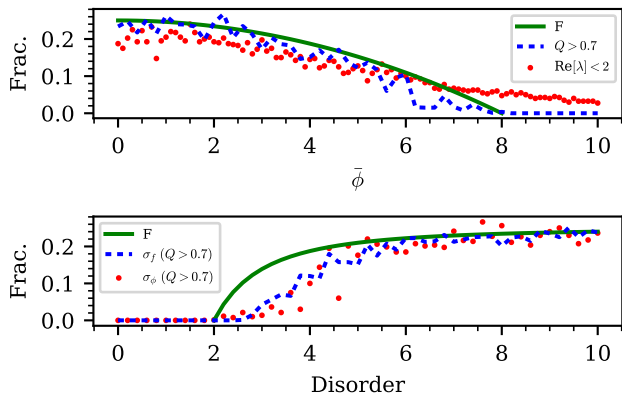
FIG. 10. **The floor-level occupation. (a)** The fraction of floor-level eigenstates drops down from 25% as $\bar{\phi}$ is increased. Floor-level eigenstates are defined as those that have $Q > 0.7$. This is compared with F from Eq.(25), and with the number of states with Re$[\lambda] < 2$ ($\sigma_\phi = 8$). **(b)** The fraction of floor-level eigenstates versus σ_f and σ_ϕ. The average propulsion is $\bar{\phi} = 2$.

this fraction becomes

$$F_{\text{floor}} = \frac{(\sigma_\phi - \bar{\phi})(\sigma_\phi + \bar{\phi})}{4\sigma_\phi^2} \qquad (25)$$

Consequently, as the disorder is increased we expect a crossover from band-structure implied occupation to floor-level implied occupation as illustrated in Fig.10(a).

Summarizing the TSD case (with zero average propulsion) we realize that in the absence of disorder, the low lying eigen-modes are real and non-helical, because they all belong to a single-channel symmetric mode $|k, +\rangle$ of Eq.(15) with $\varphi = 0$. Increasing the disorder strength, the low lying eigen-modes occupy only the floor level, hence become helical (2 sites with the same n cannot both serve as sinks), and therefore remain real. Note however that we cannot exclude that what we call here "real" possesses a very small imaginary part due some residual hopping. On the basis of the numerics it is difficult to obtain a conclusive statement, but from practical (physical) point of view such conclusive statement is of no importance.

The same calculation of Eq.(25) holds if we have CSD instead of TSD, namely, with σ_ϕ replaced by σ_f. See Fig.10(b). In contrast with the TSD case, in the strong CSD limit, we do not expect the floor-band to be restricted to the region Re$[\lambda] \in [0, 2]$. This follows from the fact that in the extreme case, for $\sigma_f \gg \bar{\phi}$, the system has a mirror symmetry, so that the two floor-band are separated by $\Delta\lambda = 2$ along the real λ axis. It follows that in this limit, the fraction of states within Re$[\lambda] \in [0, 2]$ is approximately 12.5%.

VII. THE TOPOLOGICAL INDEX

The *bulk-edge correspondence* principle suggests that localized states should appear at interfaces, connecting regions of the sample characterized by a different topological number. Below we illuminate the relation between this statement, and the floor-level phenomenology that has been introduced in the previous section.

A translationally invariant sample can be characterized by the winding number

$$w = \frac{1}{2\pi i} \int_0^{2\pi} dk \frac{d}{dk} \ln\left(\det\left[W^{(k)}\right]\right), \qquad (26)$$

which counts the number of times that the eigenenergies encircle the zero energy. Similar to the case of a vanishing band-gap in the Hermitian case, the winding number is ill defined when dealing with a conservative system, that always has a $\lambda = 0$ eigenvalue. To circumvent this problem, following [20, 21], one has to introduce an F-bias, as explained in Appendix B.

Considering an interface between two bulk regions "L" and "R" the topological index is defined as

$$\delta w = w_L - w_R \qquad (27)$$

The interface will localize left (right) zero-energy edge-modes, if in some finite neighborhood of $F = 0$, the index δw is positive (negative) independently of F. It is important to realize that two bands are not required for observing topological phenomena in non-hermitian Hamiltonian, which stands in contrast with Hermitian systems [19].

In Appendix B we calculate the topological number of a translationally invariant system given by Eq.(7). We find that a non-zero topological index is associated with interfaces between regions with opposite drift field, independent of the self propulsion. We further observe that probability density can accumulate also at interfaces between regions that have the same topological number. We point out (see last paragraph of Appendix B) that the localization in the latter case is less pronounced, and diminishes if the length of the non-disordered regions is increased.

The above observations lead to the conclusion that CSD is more effective (compared with TSD) in introducing localized states. The implication of this observation is demonstrated in Fig.8. We see in panel (b) a remarkable increased in the likelihood to observe eigen-modes with small M. Another way to phrase this conclusion is to say that eigen-modes that reside in the floor level tend to localize if CSD is dominating, and tend to be more extended if TSD is dominating.

VIII. SUMMARY AND DISCUSSION

The relaxation modes of a stochastic network can be either over-damped or under-damped depending on whether their λ-s are real or complex. In a non-active unbiased disordered network, say a ring, the relaxation is over-damped. But if we add bias (finite $\bar{f}$) the low modes become delocalized and we can have under-damped relaxation, which is associated with correlated currents over the whole ring.

The picture of relaxation is much richer if we consider an active network. Without disorder the self-propelled motion (finite $\bar{\phi}$) implies that above a critical value (ϕ_c) the relaxation modes become helical due to topological symmetry breaking.

Once disorder is taken into account the picture changes dramatically. An emergent feature of active networks is a novel type of disorder - TSD. Random ϕ_n, unlike uniform ϕ_n, does not require a finite threshold to induce complexity in the spectrum.

We have presented a detailed investigation of the Fourier-Laplace spectrum for a minimal model of an active network Fig. 1. A time-domain illustration of the dynamics is displayed in Fig. 11. This illustration shows how the under-damped relaxation due to self-propulsion is blurred by the introduction of disorder. Our objective was to provide a quantitative analysis for this dynamical behavior.

A few remarks are in order: **(1)** If the average self-propulsion is zero, the effect of CSD is to stabilize the reality of the spectrum, while TSD induces complexity in the central part of the spectrum via band-mixing. **(2)** If we further increase the stochastic disorder the fraction of complex eigen-modes become smaller. There are two issues here: the formation of the floor-level due to the effective dilution of the lattice; and the fragmentation of the lattice into smaller regions that support the localized eigen-modes. **(3)** Opposing to the common perspective that ties between delocalization and complexity in a single channel system [10], TSD both makes the spectrum complex and localizes the states. **(4)** The effect of TSD can be distinguished from the effect of CSD also if the average self-propulsion is not zero (finite $\bar{\phi}$). The CSD affects democratically all the under-damped modes, while the TSD has larger effect on the more localized modes.

We can adopt a more general perspective with regard to the floor-level phenomenology, that can be applied for any active network. Strong stochastic disorder, irrespective of its nature, induces *lattice dilution*, leading to the formation of a floor-level that is spanned by the sites that serve as sinks for the stochastic flow. Consequently the effective dimensionality of the lattice reduces. In our geometry the floor-level sites form a single channel chain, hence a robust reality is gained within the floor-level band.

The floor level consists of local sinks of the stochastic flow. In particular local sinks appear at interfaces between segments characterized by a different *topologi-*

cal numbers that are determined by the sign of the drift flow, irrespective of the self-propulsion. Still, we observe that probability density can accumulate at interfaces between regions that have the same topological number, e.g. in the presence of TSD and uniform drift. Our numerical analysis shows that the degree of localization in the latter case is less pronounced and smeared away if the non-disordered regions are lengthy. This observation highlights the role of topological protection and its implication on localization in non-equilibrium stochastic flow.
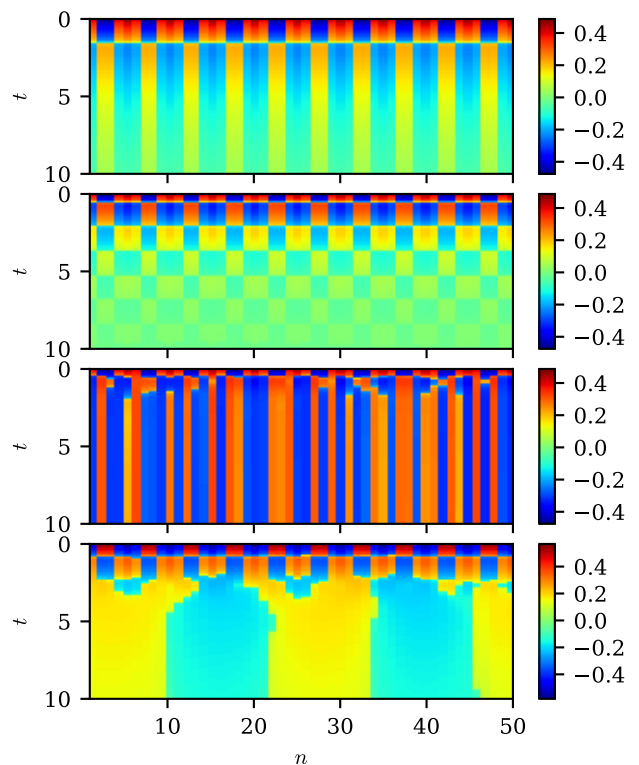

FIG. 11. **Simulation of polarization as a function of time.** The polarization $D_n(t)$ as defined in Eq. (9) is imaged as a function of time. In all the panels the initial perpetration is a modulated density with $k = 2\pi/5$. Only 50 sites are displayed. **(a)** Over-damped oscillations for $\sigma_\phi = 0.5$ are observed since the self-propulsion is below the critical threshold. **(b)** For $\sigma_\phi = 2$, which is above the threshold, one observes under-damped relaxation due to topological symmetry breaking. **(c)** Once disorder is added, the non-uniform NESS pattern overtakes almost immediately. Parameters here are as in Fig. 2. **(d)** In the latter case we provide an image of the time derivative $\dot{D}$, hence one can resolve how the under-damped relaxation is blurred. For presentation purpose the color-code has been scaled.

Appendix A: The W matrix

The matrix $\boldsymbol{W}$ can be regarded as the representation of a non-hermitian Hamiltonian. It consist of 3 terms:

$$\boldsymbol{W} = \boldsymbol{W}_{\text{flip}} + \boldsymbol{W}_{\text{hop}} - \sum_{n,y} |n,y\rangle \, \gamma_{n,y} \, \langle n,y|$$

Using the Dirac's bra-ket notations, the explicit expressions for the flipping and hopping terms are

$$\boldsymbol{W}_{\text{flip}} = \sum_{n} |n,\uparrow\rangle\langle n,\downarrow| + |n,\downarrow\rangle\langle n,\uparrow|$$

$$\boldsymbol{W}_{\text{hop}} = \sum_{n,y} |n{+}1,y\rangle\langle n,y| \, e^{\frac{\mathcal{E}_{n,y}}{2}} + |n,y\rangle\langle n{+}1,y| \, e^{-\frac{\mathcal{E}_{n,y}}{2}}$$

with $\mathcal{E}_{n,y}$ that are given by Eq.(3). The decay rate are implied by conservation of probability:

$$\gamma_{n,y} = 1 + e^{\mathcal{E}_{n,y}/2} + e^{-\mathcal{E}_{n-1,y}/2} \tag{A1}$$

The translation operators $e^{\pm i\boldsymbol{p}}$ of Eq.(7) are defined by $e^{\mp i\boldsymbol{p}} |n,y\rangle = |n{\pm}1,y\rangle$. The $\boldsymbol{\sigma}_i$ operators are defined by $\langle n,y'| \, \boldsymbol{\sigma}_i \, |n,y\rangle = (\sigma_i)_{y'y}\delta_{n'n}$ in terms of Pauli matrices.

Appendix B: The non-disordered spectrum

Pedagogically it is useful to consider a single-channel tight binding model, which is biased by stochastic field f. Additionally we introduce an F-bias [20, 21], which affects the off-diagonal rates, but not the diagonal elements. Accordingly

$$\boldsymbol{W} = -2\cosh\left(\frac{f}{2}\right) + \sum_{\pm} e^{\pm\left(\frac{f}{2}+F\right)} \, e^{\mp i\boldsymbol{p}} \tag{B1}$$

The Bloch spectrum is $\{-\lambda_k\}$ with

$$\lambda_k = 2\cosh\left(\frac{f}{2}\right) - 2\cosh\left(\frac{f}{2}+F\right)\cos(k)$$
$$+ i2\sinh\left(\frac{f}{2}+F\right)\sin(k)$$

This spectrum goes through the origin for $F = 0$, which reflects the existence of the NESS for a conservative matrix. But for any non-zero F we can define the winding number w of the $-\lambda_k$ trajectory relative to the origin. Namely,

$$w = \text{sign}\left[|f + 2F| - f\right] \tag{B2}$$

If we have two regions (left and right) that do not have the same f, the difference $\delta w \equiv w_L - w_R$ is well defined in the limit $F \to 0$ and does not depend whether we take the limit from the positive or from the negative side. For the topological index of Eq.(27) we get $\delta w = 1$. By the *bulk-edge correspondence* principle it is implied that a bound state should reside at one of the two interfaces between the two bulk regions which acts as a sink for the
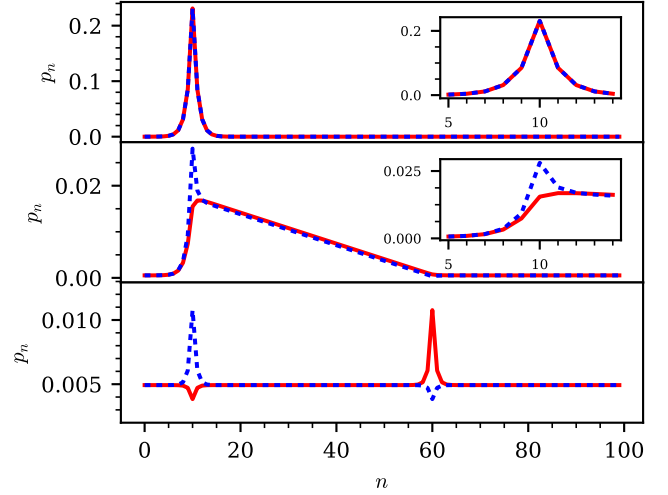

FIG. 12. The NESS for a system that is composed of two regions. The probabilities on the upper and lower chains are plotted in dashed-blue and solid-red lines. **(a)** The two regions are with opposite f. The sink interface is located at $n{=}10$, while the other interface is at $n{=}60$. **(b)** The $[10,60]$ region is with ϕ only, and the other region is with f only. **(c)** The two regions are with opposite ϕ. Strong localization near the interface is observed only in case (a) where the topological index is non-zero.

flow. (We assume periodic boundary conditions, so the interface is in fact two locations along the ring.)

We now can consider on equal footing our model system Eq.(7). Here the winding number is calculated from the 2×2 matrix $\boldsymbol{W}^{(k)}$. As in the single-channel example the topological-index calculation requires to introduce an F-bias. The resulting matrix reads:

$$\boldsymbol{W}^{(k)} = b\sigma_x + 2\cosh\left(\frac{f + \phi\sigma_z}{2} + F - ik\right)$$
$$- b - 2\cosh\left(\frac{f + \phi\sigma_z}{2}\right) \tag{B3}$$

with eigenvalues $\{-\lambda_k\}$, where

$$\lambda_{k,s} = b - 4\cosh\left(\frac{\phi}{2}\right)\sinh\left(\frac{f{+}F{-}ik}{2}\right)\sinh\left(\frac{F{-}ik}{2}\right)$$
$$\mp \sqrt{b^2 + 16\sinh\left(\frac{\phi}{2}\right)^2\cosh\left(\frac{f{+}F{-}ik}{2}\right)^2\sinh\left(\frac{F{-}ik}{2}\right)^2}$$

where $s = 1, 2$ corresponds to $\mp$. Note consistency with Eq.(B1) upon the substitution $b = \phi = 0$. The spectrum in a few representative cases has been illustrated in Fig.4. The $\pm k$ degeneracy is removed if we add a non-zero f in a way that is very similar to the single-channel analysis. This has been demonstrated in Fig.4(c). With an additional F-bias the loop looks similar but does not go through the origin. Our analysis shows that the presence of a finite self propulsion does not alter the topological index. Namely, the expression for w is Eq.(B2) as for a single chain.

If we have an interface between two regimes, that do not have the same (f, ϕ) bias, there is still a possibility to observe interface-states, even if the topological-index is zero. This is demonstrated in Fig. 12. We see there that strong localization near the interface is observed only in panel (a) where the $\delta w \neq 0$. In panel (b) the high-probability interface and the low probability interface are mediated by a linear variation in the zero drift $(f = 0)$ region, as in Ohmic systems. In panel (c) the sink in one chain is in-fact a saddle, due to its coupling to the other chain, hence the localization is weak. If a longer sample is taken, the hump in panel (c) is smeared out (not shown).

Appendix C: Linear algebra of non-Hermitian matrices

A non-hermitian operator $\boldsymbol{A}$ has right-eigenvectors that satisfy $\boldsymbol{A}|x\rangle = \lambda_x|x\rangle$. Where $|x\rangle$ is chosen to have the normalization $\langle x|x\rangle = 1$. These eigenvectors are in general non-orthogonal: $\langle x|y\rangle \neq 0$. To any right-eigenvector we can associate left-eigenvector through the adjoint operator: $\boldsymbol{A}^\dagger|\tilde{x}\rangle = \lambda_x^*|\tilde{x}\rangle$. The right- and left-eigenvectors form a bi-orthogonal set and we choose the normalization of the left-eigenvectors such that $\langle\tilde{x}|y\rangle = \delta_{x,y}$. For a complete basis $\mathbf{1} = \sum_x |x\rangle\langle\tilde{x}|$. The matrix representation $B_{y,x}$ of an operator $\boldsymbol{B}$, in the basis $|x\rangle$ is defined via $\boldsymbol{B}|y\rangle = \sum_x B_{x,y}|x\rangle$. One deduces that $B_{x,y} = \langle\tilde{x}|\boldsymbol{B}|y\rangle$, and $\boldsymbol{B} = \sum_{x,y}|\tilde{y}\rangle B_{x,y}\langle x|$.

Given a non-hermitian matrix $\boldsymbol{H}_0$ and some perturbation $\boldsymbol{V}$, we define the right and left unperturbed eigenvectors $|n\rangle$ and $\langle\tilde{m}|$. In this basis $\boldsymbol{H}_0$ is diagonal with eigenvalues $\lambda_n^{(0)}$. The perturbed eigenvalues in second order are [33]:

$$\lambda_n = \lambda_n^{(0)} + \lambda_n^{(1)} + \lambda_n^{(2)} \tag{C1}$$

$$\lambda_n^{(1)} = \langle\tilde{n}|\boldsymbol{V}|n\rangle \tag{C2}$$

$$\lambda_n^{(2)} = \sum_m \frac{\langle\tilde{n}|\boldsymbol{V}|m\rangle\langle\tilde{m}|\boldsymbol{V}|n\rangle}{\lambda_n^{(0)} - \lambda_m^{(0)}} \tag{C3}$$

Note that $V_{n,m}$ will take different forms depending on the normalization of the basis, while the product $V_{n,m}V_{m,n}$ is independent of normalization due to the bi-orthornormality.

[1] P. Romanczuk, M. Bär, W. Ebeling, B. Lindner, and L. Schimansky-Geier, The European Physical Journal Special Topics 202, 1 (2012).
[2] A. Thompson, J. Tailleur, M. Cates, and R. Blythe, Journal of Statistical Mechanics: Theory and Experiment 2011, P02029 (2011).
[3] Y. Katz, K. Tunstrøm, C. C. Ioannou, C. Huepe, and I. D. Couzin, Proceedings of the National Academy of Sciences 108, 18720 (2011).
[4] M. C. Marchetti, J.-F. Joanny, S. Ramaswamy, T. B. Liverpool, J. Prost, M. Rao, and R. A. Simha, Reviews of Modern Physics 85, 1143 (2013).
[5] A. Walther and A. H. Muller, Chemical reviews 113, 5194 (2013).
[6] P. M. Wheat, N. A. Marine, J. L. Moran, and J. D. Posner, Langmuir 26, 13052 (2010).
[7] A. M. Menzel, Physics reports 554, 1 (2015).
[8] M. Berry, Czechoslovak Journal of Physics 54, 1039 (2004).
[9] C. M. Bender, Reports on Progress in Physics 70, 947 (2007).
[10] N. Hatano and D. R. Nelson, Phys. Rev. Lett. 77, 570 (1996).
[11] N. Hatano and D. R. Nelson, Phys. Rev. B 56, 8651 (1997).
[12] N. M. Shnerb and D. R. Nelson, Physical review letters 80, 5172 (1998).
[13] J. Feinberg and A. Zee, Phys. Rev. E 59, 6433 (1999).
[14] Y. Kafri, D. K. Lubensky, and D. R. Nelson, Biophysical Journal 86, 3373 (2004).
[15] Y. Kafri, D. K. Lubensky, and D. R. Nelson, Phys. Rev. E 71, 041906 (2005).
[16] A. Amir, N. Hatano, and D. R. Nelson, Physical Review E 93, 042310 (2016).
[17] D. Hurowitz and D. Cohen, Scientific reports 6 (2016).
[18] D. Hurowitz and D. Cohen, Phys. Rev. E 93, 062143 (2016).
[19] Z. Gong, Y. Ashida, K. Kawabata, K. Takasan, S. Higashikawa, and M. Ueda, arXiv:1802.07964 (2018).
[20] A. Murugan and S. Vaikuntanathan, Nature communications 8, 13881 (2017).
[21] K. Dasbiswas, K. Mandadapu, and S. Vaikuntanathan, arXiv:1706.04526 (2017).
[22] C. Kane and T. Lubensky, Nature Physics 10, 39 (2014).
[23] T. Reichenbach, T. Franosch, and E. Frey, Physical review letters 97, 050603 (2006).
[24] D. Helbing, Reviews of modern physics 73, 1067 (2001).
[25] F. J. Dyson, Phys. Rev. 92, 1331 (1953).
[26] T. A. L. Ziman, Phys. Rev. Lett. 49, 337 (1982).
[27] Y. G. Sinai, Theory of Probability & Its Applications 27, 256 (1983).
[28] B. Derrida, Journal of Statistical Physics 31, 433 (1983).
[29] J.-P. Bouchaud, A. Comtet, A. Georges, and P. Le Doussal, Annals of Physics 201, 285 (1990).
[30] J.-P. Bouchaud and A. Georges, Physics Reports 195, 127 (1990).
[31] S. Alexander, J. Bernasconi, W. Schneider, and R. Orbach, Reviews of Modern Physics 53, 175 (1981).
[32] W. Chan, X. Wang, and X. C. Xie, Physical Review B 54, 11213 (1996).
[33] M. M. Sternheim and J. F. Walker, Physical Review C 6, 114 (1972).